



# The 2.6–2.3 ka explosive eruptive period of the Pululahua dome complex, Ecuador: insights from pyroclast analysis

Anais Vásconez Müller<sup>1</sup> · Katharine V. Cashman<sup>1,2</sup> · Samuel J. Mitchell<sup>1</sup> · Francisco J. Vasconez<sup>1,3</sup>

Received: 9 March 2022 / Accepted: 16 July 2022 / Published online: 3 August 2022  
© International Association of Volcanology & Chemistry of the Earth's Interior 2022

## Abstract

Pululahua is an active volcano located 15 km north of Quito, Ecuador, that comprises sixteen dacitic-andesitic lava domes and a 13 km<sup>2</sup> sub-rectangular depression formed between ~2.6 and ~2.3 ka. We use a detailed study of 70 flow and fall deposits that make up the pyroclastic sequence to show that the depression, previously classified as a caldera, was formed by numerous Vulcanian to (sub-) Plinian eruptions that destroyed both earlier and co-eruptive lava domes. We support this interpretation with field work, analysis of grain size distributions, density and components of 24 key deposits, supplemented by textural and petrologic analyses of 16 juvenile pyroclasts from throughout the pyroclastic sequence. These data document an alternation of (sub-) Plinian and Vulcanian eruptions dominated by denser juvenile material that preserves microtextural variations indicating changes in shallow level magma storage accompanying Vulcanian explosions. An exploratory examination of phenocryst textures and plagioclase and amphibole rim compositions suggests that much of the eruptive activity was driven by repeated inputs of less evolved magma into the Pululahua magmatic system. The inferred sequence of events provides a new hypothesis for the formation of the current morphology of Pululahua, including multiple episodes of both effusive and explosive eruptions accompanied by vent migration. Our findings offer an important insight into Pululahua's potential future hazard scenarios, which could affect millions of people.

**Keywords** Lava dome complex · Vulcanian eruptions · (Sub-) Plinian eruptions · Componentry · GSD · Textural analysis

## Resumen

El Pululahua es un volcán activo situado 15 km al norte de Quito, Ecuador, que comprende dieciséis domos de lava dacítica-andesítica y una depresión sub-rectangular de 13 km<sup>2</sup> formada entre ~2,6 y ~2,3 mil años atrás. En este artículo realizamos un estudio detallado de 70 depósitos de flujos y caídas que componen la secuencia piroclástica para mostrar que la depresión, previamente clasificada como caldera, se formó en realidad por numerosas erupciones Vulcanianas a (sub-) Plinianas que destruyeron domos de lava pre-existentes y co-eruptivos. Fundamentamos esta interpretación con trabajo de campo, el análisis de densidad, componentes y distribución del tamaño de grano de 24 depósitos clave, además del análisis textural y petrológico de 16 piroclastos juveniles muestreados a lo largo de toda la secuencia. Los datos documentan una alternancia entre erupciones (sub-) Plinianas y Vulcanianas. La predominancia de material juvenil denso que conserva variaciones

---

Editorial responsibility: U. Kueppers

---

This paper constitutes part of a topical collection:

What pyroclasts can tell us

---

✉ Anais Vásconez Müller  
anaisvasconez@gmail.com

<sup>1</sup> School of Earth Sciences, University of Bristol, Bristol BS8 1RJ, UK

<sup>2</sup> Department of Geological Sciences, University of Oregon, Eugene, OR 97403-1272, USA

<sup>3</sup> Instituto Geofísico, Escuela Politécnica Nacional, Ladrón de Guevara E11-253, Quito, Ecuador

microtexturales dentro de los depósitos Vulcanianos indica cambios en el almacenamiento de magma a poca profundidad antes de estas erupciones. Un análisis exploratorio de las texturas de los fenocristales y de las composiciones de los bordes de plagioclasa y anfíbol sugiere que gran parte de la actividad eruptiva fue desencadenada por repetidas inyecciones de magma menos diferenciado al sistema magmático del Pululahua. La secuencia inferida de eventos eruptivos entre ~2,6 y ~2,3 mil años proporciona una nueva hipótesis para la formación de la actual morfología del Pululahua, incluyendo múltiples episodios de erupciones efusivas y explosivas acompañadas de la migración de los ventos eruptivos. Nuestros resultados aportan una nueva interpretación de los posibles futuros escenarios de peligro asociados al volcán Pululahua, los cuales podrían afectar a millones de personas.

## Introduction

The Pululahua dome complex is one of twenty-four active volcanoes in Ecuador (Ramon et al. 2021), where volcanism is driven by oblique subduction of the oceanic Nazca plate underneath the South American plate (Gutscher et al. 1999; Witt et al. 2006; Nocquet et al. 2014) (Fig. 1a). Pululahua is located in the Western Cordillera of the Ecuadorian Andes, 15 km north of the capital, Quito. It comprises sixteen dacitic to andesitic lava domes and a 4 km wide and 300 m deep sub-rectangular depression (Fig. 1b, c). The eruptive history of this dome complex, described in detail in Andrade et al. (2021), is divided into four major geological units: Units I and II include 13 dacitic lava domes that erupted in the late Pleistocene ( $> 18\text{--}11$  ka) and their associated block-and-ash-flow (BAF) deposits (Fig. 1b, c). Unit III comprises flow and fall deposits ( $0.58 \pm 0.25$  km<sup>3</sup> DRE) emplaced between ~2.6 and ~2.3 ka; charcoal-rich layers in Unit III indicate three breaks in eruptive activity long enough for substantial vegetation growth that subdivide the ~300 years of explosive activity into four major eruptive episodes (E1 to E4 in Andrade et al. 2021, Fig. 1b, d). Eruptive activity at Pululahua culminated with effusive growth of three intra-depression domes at ~2.24 ka (Unit IV) and the accompanying emplacement of BAF deposits (Fig. 1b, c).

Pululahua has been referred to as a volcanic caldera (Papale and Rosi 1993; Padrón et al. 2008; Volentik et al. 2010; Smithsonian Institution 2021), even though the formation mechanism of the depression has not been previously investigated. Papale and Rosi (1993) were the first to study Pululahua's explosive deposits in detail. They focused on an extensive pumice fall deposit from the initial stages of Unit III (E1-B in Fig. 2), for which they calculated a DRE volume of 0.34 km<sup>3</sup> and a Volcanic Explosivity Index

(VEI) of 4. This work has been extended by Volentik et al. (2010) to estimate the Plinian column height ( $30 \pm 3$  km) and eruption duration ( $72 \pm 47$  min) based on inversion models. This well-studied pumice fall deposit immediately succeeds a fine dense-clast-rich ash layer that initiated the explosive sequence of Unit III (Papale and Rosi 1993, E1-A in Fig. 2). Similar stratigraphic sequences of an initial fine lithic-rich ash followed by a major pumice lapilli fall deposit are observed, among others, for the 0.65 ka Mt Pelée eruption (Villemant et al. 1996; Villemant and Boudon 1998), the 1902 La Soufrière eruption (Cole et al. 2019), the Shinmoedake eruption in 2011 (Miyabuchi et al. 2013) and the 2014 Kelud eruption (Maeno et al. 2019). Previous work suggests that deposit sequences of this type are generally formed by lithostatic load reduction, sometimes influenced by interaction with influxes of sub-surface water (Heiken and Wohletz 1987) that cause the sudden depressurisation of a deeper seated, volatile-rich magma body (Castro and Gardner 2008; Preece et al. 2016; Massaro et al. 2018).

Importantly, recent work (Andrade et al. 2021) has demonstrated that several BAF deposits located to the northwest of Pululahua (Guarumal and Tanachi terraces in Fig. 1b) could not have originated from the existing domes and that the two smaller intra-depression structures — El Chivo I and II — are dome-conduit remnants that belong to Unit II (Fig. 1b, c) rather than being post-depression domes, as previously thought (Águila 1986; Papale and Rosi 1993). Based on these observations, Andrade et al. (2021) suggested the existence of prior domes that were (partially) destroyed during the explosive events of Unit III. Globally, the growth and destruction of ephemeral domes as part of explosive sequences has been documented at Novarupta 1912 (Adams et al. 2006), Mount St. Helens 1980 (Christiansen and Peterson 1981), Redoubt 1989 (Gardner et al. 1994), Soufriere Hills Volcano 1995–2010 (Wadge et al. 2014), Merapi 2010 (Preece et al. 2016) and La Soufrière (St. Vincent) in 2021 (Global Volcanism Program 2021). Associated juvenile deposits formed by Vulcanian (dome growth) and sub-Plinian (dome destruction) eruptions typically include pumice, moderately vesicular dacites or andesites and dense dome material (Heiken and Wohletz 1987; Cashman and McConnell 2005; Adams et al. 2006; Wright et al. 2007; Giachetti et al. 2010; Miyabuchi et al. 2013). Explosive dome destruction can initiate by (i) injection of new magma from below (Heiken and Wohletz 1987), (ii) exceedance of a critical overpressure beneath the young dome (Druitt et al. 2002; Wright et al. 2007; Preece et al. 2016) or (iii) gravitational collapse of the dome and subsequent downward decompression (Miller 1994). Inclusion of older lithics within a pumiceous sequence may indicate opening of new vents (Lavallée et al. 2012) or the destruction of young but not co-eruptive domes (Maeno et al. 2019).

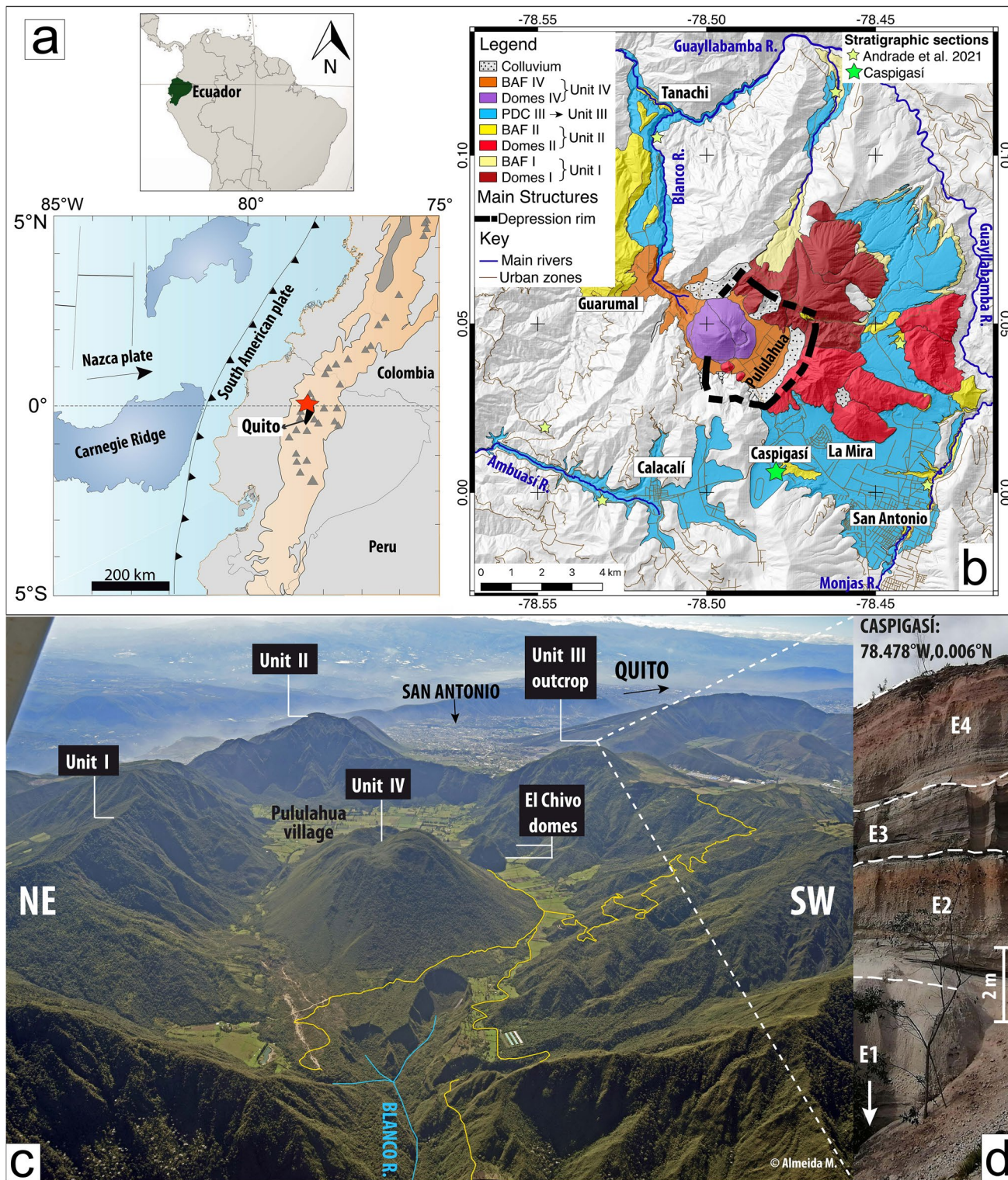
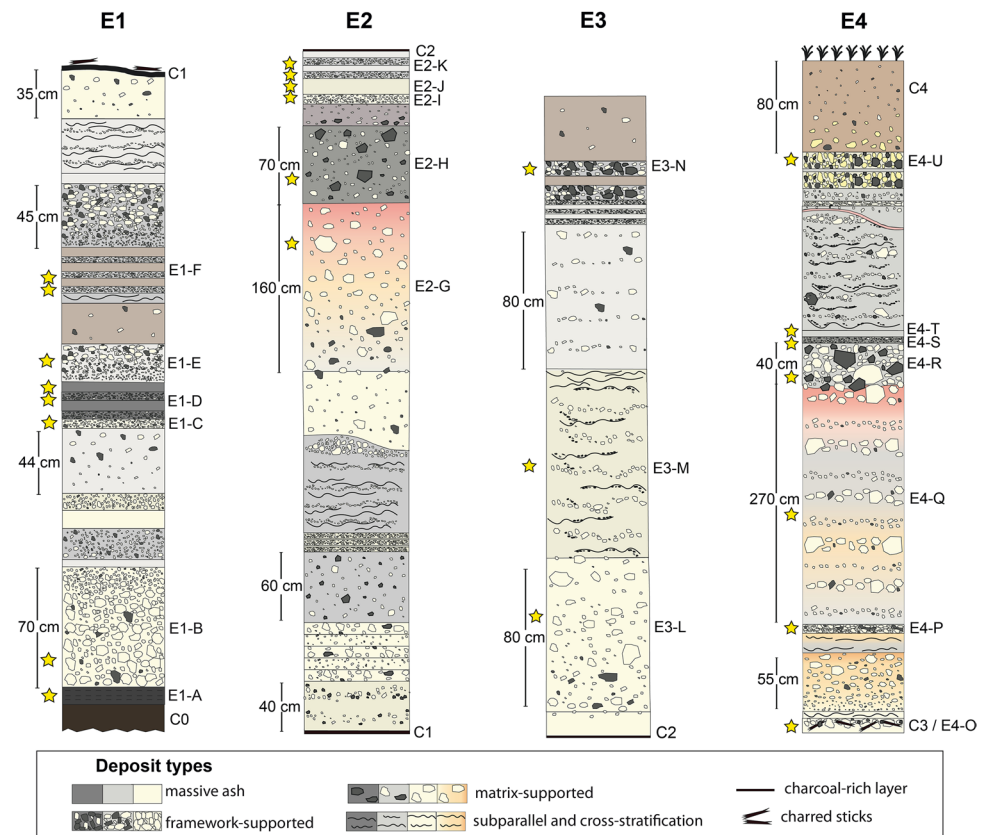


**Fig. 1** (a) Geotectonic setting of Ecuador. Grey triangles represent Quaternary volcanoes of the Andean range (light orange); Pululahua is indicated by the red star, Quito is the black polygon. (b) Simplified geological map of Pululahua and its eruptive deposits; bright green star indicates the location of the here-analysed stratigraphic section,

modified from Andrade et al. 2021. (c) Pululahua seen from the NW. Units I — IV and El Chivo dome-conduit remnants are labelled; main access roads in yellow. (d) Quarry exposing explosive deposits of Unit III to the SSE of Pululahua; white dashed lines indicate charcoal-rich bioturbated layers

**Fig. 2** Digitalised stratigraphic columns for pyroclastic deposits of Unit III. Yellow stars denote sampled layers. C1, C2 and C3 are charcoal-rich layers that subdivide Unit III into four eruptive episodes E1–E4. Note that each section has its own vertical scale



Eruptive style transitions between explosive and effusive eruptions are common at dome-forming volcanoes, including Pululahua's neighbours in the Western Cordillera Guagua Pichincha (Robin et al. 2008), Mojanda-Fuya Fuya (Robin et al. 1997, 2009) and Cotacachi-Cuicocha (Pidgen 2014; Almeida 2016). Specifically, transitions from explosive to effusive activity (Cassidy et al. 2018) have been attributed to (i) loss of reservoir pressure and consequent reduced magma ascent (Nguyen et al. 2014), (ii) decrease of exsolved volatile pressure by elevated gas loss (Cashman 2004; Preece et al. 2016), (iii) conduit narrowing and lateral outgassing from overpressure (Manga et al. 2018), (iv) a decline in the magma supply rate (Miller 1994) and (v) an increase in magma viscosity, and resulting decrease in magma ascent, caused by rapid crystallisation (Mujin and Nakamura 2014). Several of the aforementioned explosive eruptions, which also included ephemeral lava dome growth, culminated with the effusive emplacement of stable domes.

Understanding the nature of past eruptions at Pululahua is important for hazard assessment, as its proximity to the ever-growing capital city, Quito, means that future activity could jeopardise millions of people (Fig. 1b). The severity and extent of the negative impacts will, however, depend on the eruption style. While effusive growth of a new lava dome would have disastrous consequences locally, paroxysmal explosive activity of the magnitude recorded between

2.6 and 2.3 ka could affect the entire capital. Studying Pululahua's explosive sequence in more detail is therefore an essential first step towards improving future hazard assessment, updating Pululahua's hazard map (Hall and Hillebrandt 1988) and enhancing monitoring efforts. The aim of this manuscript is to present a detailed study of the entirety, and variety, of deposits within the Unit III pyroclastic sequence using grain size distribution (GSD), componentry, textural and petrological analyses; we use these data to propose a new hypothesis for the origin of Pululahua's 4 km wide sub-rectangular depression and to assess the role played by eruptive style transitions.

## Materials and methods

Two field campaigns were undertaken in March and July 2020 to characterise the pyroclastic sequence of Unit III. Both campaigns were conducted at an abandoned quarry behind the village of Caspigasí (78.478°W, 0.006°N, Fig. 1b, d). This single outcrop at 2.5 km from Pululahua's SSE crater rim was chosen as, out of the 7 stratigraphic sections previously studied by Andrade et al. (2021) (Fig. 1b), it most completely exposes the entire eruptive sequence (70 pyroclastic deposits) of Unit III. This outcrop allowed us to conduct a detailed description of the entire stratigraphic sequence and to take samples

of 24 selected deposits. Marker layers include a dark brown palaeosol that underlies the explosive deposits (C0 in Fig. 2), three charcoal-rich layers (C1, C2 and C3) that separate the four explosive episodes (E1 to E4) and a light brown soil that caps the pyroclastic sequence (C4 in Fig. 2).

Previous studies have demonstrated that GSD and componentry analysis provide critical data for distinguishing lithofacies of pyroclastic deposits and identifying discrete vent-opening events (Lavallée et al. 2012), vent erosion and widening (Maeno et al. 2019) and ephemeral dome growth and destruction during explosive eruptive phases (Adams et al. 2006; Preece et al. 2016). We used these two key methodologies, combined with textural and petrological analyses, to create a detailed stratigraphic record of the eruptive events at Pululahua from ~2.6 to ~2.3 ka.

### GSD analysis and componentry classification

In the field, we described layer thickness and colour, degree of deposit consolidation, matrix abundance, sedimentary structures (stratification and grading), overall sorting (minimum to maximum clast size) and overall clast shape, and roughly estimated the proportions of juvenile material, as well as accidental fragments, for clasts larger than 5 mm based on their colour, shape and degree of vesiculation. These field observations were collected for each of the 70 pyroclastic deposits and are presented in the Supplementary Material 1, Table ESM-1.1.

Twenty-four of the 70 deposits were sampled through their full height, with bulk sample weight from thicker deposits reaching 3000 g and thin deposit samples weighing between 150 and 350 g. All samples were sieved manually at  $1\phi$  steps ( $\phi = -\log_2 d$ , with  $d$  being the particle diameter in mm) from  $-7\phi$  to  $4\phi$  (128 mm to 63  $\mu\text{m}$ ); fine fractions were analysed to  $10\phi$  (1  $\mu\text{m}$ ) using a laser scattering particle size distribution analyser Horiba LA-960 at the Instituto Geofísico – Escuela Politécnica Nacional (IG-EPN), Ecuador. For the latter, three measurements were performed on 0.1 g of each sample in deionised water to ensure reproducibility. We used the real and imaginary refractive indexes reported in Vogel et al. (2017) for dacitic compositions, which correspond to a theoretical density of 2.6  $\text{g}/\text{cm}^3$ , which is only 0.15  $\text{g}/\text{cm}^3$  higher than the DRE density estimated for Pululahua Unit III rocks by Andrade et al. (2021). Sieve and laser data were later combined assuming similar densities for the fine (< 63  $\mu\text{m}$ ) fraction (comparable weight and volume percent).

Clasts between  $-7\phi$  and  $-1\phi$  were classified based on their colour, vesicularity, shape and qualitative density until all, or at least 300, randomly selected clasts of each fraction had been analysed. Since laboratory equipment was not available during COVID-19 lockdowns, we developed a relative density scale for larger clasts by dropping

them individually into a bowl of water and observing their sinking behaviour. Four categories describe this behaviour: *floats* (> 3 s), *sinks slowly* (after floating for ~1 s), *sinks* and *sinks fast* (instantly upon submergence). Both the qualitative density observations and the visual characteristics were used to classify each clast as (i) *highly vesicular pumice (HVP)* (floats/sinks slowly, white/beige, vesicular), (ii) *medium vesicular pumice (MVP)* (sinks, beige/light grey, smaller or fewer vesicles), (iii) *low vesicular clast (LVC)* (sinks/sinks fast, grey, irregular vesicles), (iv) *dense dome clast (DDC)* (sinks fast, grey/dark grey, crystalline, no visible vesicles, blocky), (v) *oxidised clast (Ox)* (sinks fast, pink to red matrix), (vi) *hydrothermally altered clast (Alt)* (sinks fast, green/yellow/orange matrix), (vii) *basement clast (B)* (sinks fast, dark grey/green, aphanitic or with quartz veins), or (viii) *free crystals (C)* (sinks, crystalline, generally plagioclase or amphibole). Component proportions for all fractions <  $0\phi$  were weighed, combined and normalised to calculate the total componentry of each deposit. Component proportions per fraction and sample can be found in the Supplementary Material 1, ESM-1.2.

### Petrographic and textural analysis

Four large pyroclasts ( $-4\phi$  to  $-3\phi$ ) of each juvenile clast type (HVP, MVP, LVC, DDC) and eruptive phase (E1–E4) were subsequently analysed at the University of Bristol. In a first step, bulk clast vesicularity was calculated for initial petrographic and microtextural observations of the selected clasts applying the paraffin method of Houghton and Wilson (1989) and using dense rock equivalent (DRE) density of 2.46  $\text{g}/\text{cm}^3$  reported in Andrade et al. (2021) for Pululahua Unit III rocks. Clasts were then mounted in epoxy and polished for textural and petrographic analysis. Backscattered electron images (BSE) of clasts were acquired using a Hitachi S-3500 N scanning electron microscope (SEM) at 20 kV and a 117 pixel/mm resolution; detailed microtextural BSE images were acquired at 1950 pixel/mm resolution. Whole-clast BSE images were subsequently cleaned and processed in Adobe Photoshop and FijiApp (Image J; Schindelin et al. 2012) to obtain crystal size distributions (CSDs) and clast crystallinity; a minimum measured crystal size threshold was set at 85  $\mu\text{m}$  (10-pixel resolution). 2D CSDs (as equant crystal diameters) from 85  $\mu\text{m}$  to 5 mm were measured from processed BSE images in geometric binning of  $10^{0.1}$ . Phenocrysts were imaged and analysed for major elements using a JEOL8730F Hyperprobe with a 20 kV accelerating voltage, 10nA beam current, a 1  $\mu\text{m}$  spot size and a range of minerals and oxides for calibration.

## Results

### Stratigraphy

At the Caspigasí outcrop, the entire stratigraphic column of Unit III reaches to 19 m thickness (Fig. 1d). It encompasses 70 distinct deposits including three charcoal-rich layers (C1–C3 in Fig. 2) that subdivide this pyroclastic sequence into four main episodes (E1 to E4, Andrade et al. 2021). Overall, as shown in Table 1, five lithofacies types were distinguished based on degree of compaction, sorting, grading and bedding, dominant grain size and lateral continuity of layer thickness.

In all cases, the deposit colour may range from light beige to dark grey, generally reflecting variations in component proportions, which cover the full spectrum between pumice- and dense-clast-rich. The 70 deposits vary in thickness from 0.01 to 2.7 m; some are intercalated in a repetitive and alternating manner. Here we provide a summary description of the Unit III stratigraphic section for all four episodes based on the five identified lithofacies types; a detailed description of all 70 pyroclastic deposits, depicted in Fig. 2, can be found in the Supplementary Material 1.

E1 has a total thickness of ~4 m and includes 25 distinct layers, nine of which correspond to the first lithofacies type described in Table 1, eleven to the second, three to the third, and two to the fourth one (Fig. 2). While Type I and II (framework-supported) deposits are predominant throughout E1, Type III and IV (matrix-supported) lithofacies — which sum to 1.5 m — appear more regularly in the upper half of this pyroclastic sequence. E1 is topped by a 3 cm thick bioturbated layer rich in charcoal and charred sticks (C1 in Fig. 2).

At its thickest section in this outcrop, E2 reaches 5.7 m and encompasses a total of 15 distinct deposits. Seven Type III and one Type IV deposits make up most of this pyroclastic sequence (5.3 m) and are capped by one Type II and five of six Type I lithofacies. E2 is separated from

E3 by a thin but pervasive black charcoal layer with few mm-sized charred sticks. Here, E3 reaches a thickness just over 3 m and is made up of 12 distinct layers. Similar to E2, the eight framework-supported (Type I and II) deposits found at the upper end of E3 represent only a small portion (15 cm) of the full pyroclastic sequence, while two Type III, one Type IV and one Type V deposit make up most of the E3 pyroclastic sequence.

The fourth episode (E4) starts with a 10 cm thick Type I deposit that incorporates a significant number of charred sticks. E4, which at this location is 5.7 m thick, includes 17 distinct deposits, of which three are Type I, seven Type II, four Type III and three are Type IV. Close to 1 m of this pyroclastic sequence is comprised of Type I and Type II lithofacies, while the rest are Type III and IV. Throughout this final sequence, both framework- and matrix-supported deposits are intercalated; the end of explosive eruptive activity at Pululahua is indicated by an ~80 cm thick present-day soil (Fig. 2).

The following subsections focus on the results retrieved from analysis of the 24 key deposits sampled throughout the previously described pyroclastic sequence of Unit III (yellow stars in Fig. 2). Nine of these deposits correspond to Type I, ten to Type II, four to Type III and one to Type IV lithofacies. The subscripts *c* and *f* are used to distinguish samples of coarser- and finer-grained layers of the cyclic alternating deposits of E1–D, E1–F, and E2–K (e.g. E1–D<sub>c</sub>, E1–D<sub>f</sub>). A detailed lithofacies description, as well as sorting and median grain size values and component proportions for the sampled deposits, are compiled in Table 2. In the “[Componentry and cumulative grain size distribution \(GSD\)](#)” section, we present componentry and grain size distribution of the samples, and then move on to summarise our main petrographic findings in the “[Petrography](#)” and “[Phase textures and compositions](#)” sections.

**Table 1** Description of the five lithofacies types Unit III deposits are distinguished as. The third column indicates the total number of layers of each type

Type	Lithofacies description	Layers
I	Uncompacted; moderately to poorly sorted; generally massive or subtly graded fine to coarse ash; layer thickness is laterally continuous	24
II	Uncompacted; moderately well- to poorly sorted; often graded; framework-supported; generally angular (blocks and) lapilli; layer thickness is laterally continuous	20
III	Generally uncompacted; poorly sorted; often diffusely stratified by clast abundance, size and density; ash matrix supporting rounded blocks and lapilli; layer thickness varies laterally at outcrop level	16
IV	Uncompacted; poorly sorted; laterally discontinuous thin-bedded subparallel and/or cross-bedded and/or pinch-and-swell-stratification; ash matrix supporting rounded lapilli; significant layer thickness variation at outcrop level	7
V	Densely indurated; poorly sorted; fines-poor; diffusely stratified by clast size and density; coarse-ash-matrix supporting rounded lapilli; layer thickness varies laterally at outcrop level	1

**Table 2** Description of the 24 analysed pyroclastic deposits of Pululahu Unit III in stratigraphic order (youngest on top). *Md*, median diameter of analysed samples in mm;  $\sigma\phi$ , Inman (1962) sorting coefficient in phi. Juvenile component classes are highly vesicular pumice (HVP), medium vesicular pumice (MVP), low vesicular clast (LVC), dense dome clast (DDC) and free crystals (C), while accidentally incorporated older clasts include oxidised (Ox), hydrothermally altered (Alt) and basement (B) material

Deposit name	Thickness (cm)	Colour	Lithofacies type: lithology and sedimentary structure	GSD		Componentry $\geq 2$ mm (wt%)							
				$\sigma\phi$	Md	HVP	MVP	LVC	DDC	C	Ox	Alt	B
E4-U	2 layers, 10 cm each	Yellowish grey	Type II: framework-supported, uncompact angular lapilli, massive, two laterally continuous layers separated by a 2 cm thick grey fine ash bed	2.67	5.80	32.1	23.5	11.6	31.3	0.4	0.4	0.2	0.5
E4-T	4	Grey	Type I: uncompact coarse and fine ash, subtle normal grading, layer thickness is laterally continuous	1.62	0.61	8.6	40.4	23.0	21.5	1.0	3.5	0.7	1.3
E4-S	3	Dark grey	Type II: framework-supported, uncompact angular lapilli and coarse ash, subtle normal grading, layer thickness is laterally continuous	2.19	1.85	43.8	21.8	10.7	19.9	1.1	1.5	0.0	1.1
E4-R	40	Grey	Type II: framework-supported, uncompact angular blocks and lapilli, massive, layer thickness varies slightly at outcrop level	2.57	57.00	35.8	8.1	0.6	55.1	0.2	0.1	0.0	0.1
E4-Q	270	Beige to orange, grey and red	Type III: uncompact rounded blocks and lapilli supported in an ash matrix, discontinuous subparallel and pinch-and-swell-stratification by clast abundance, size and density, gradational top contact, layer thickness varies significantly at outcrop level	2.91	1.20	61.8	19.8	16.6	1.1	0.2	0.4	0.0	0.1
E4-P	10	Beige	Type II: framework-supported, uncompact angular blocks and lapilli, massive, layer thickness is laterally continuous	2.73	2.90	31.5	30.5	12.2	21.6	1.1	2.5	0.1	0.6
E4-O	10	Beige	Type II: framework-supported, uncompact angular lapilli, massive, incorporates numerous charcoal sticks, layer thickness is laterally continuous	2.78	4.00	58.5	14.3	4.3	11.0	0.9	0.6	8.0	2.4
E3-N	2 layers, 4 cm each	Grey	Type II: framework-supported, uncompact angular lapilli, massive, two laterally continuous layers separated by a densely indurated brownish 1 cm thick fine ash layer	3.02	2.00	8.4	11.9	25.8	41.3	0.4	3.1	1.8	7.3
E3-M	100	Beige to light grey	Type IV: uncompact rounded lapilli supported in an ash matrix, discontinuous subparallel and pinch-and-swell-stratification by clast size and density, thin-bedded parallel- and cross-stratified towards the top, gradational lower contact, layer thickness varies significantly at outcrop level	2.54	0.98	46.1	11.5	17.5	13.8	0.2	6.0	1.7	3.2
E3-L	80	Beige	Type III: clast-rich, partly indurated rounded blocks and lapilli supported in an ash matrix, subordinate normal-graded lithics, gradational lower and upper contact, layer thickness varies significantly at outcrop level	3.06	1.50	71.6	6.6	9.9	9.3	0.1	1.4	0.0	1.1
E2-K fine	2 layers, 5 cm each	Light grey	Type I: uncompact coarse and fine ash, massive, intercalatedly laterally continuous parallel-bedded with E2-I coarse	3.05	0.46	4.4	22.9	38.6	27.2	0.9	1.4	2.9	1.7
E2-K coarse	2 layers, 3 cm each	Grey	Type I: framework-supported, uncompact angular lapilli and ash, subtle normal grading, intercalatedly laterally continuous parallel-bedded with E2-I fine	1.66	0.62	45.3	9.7	4.0	30.3	1.7	1.5	3.4	4.1
E2-J	12	Beige	Type I: uncompact coarse and fine ash, massive, layer thickness is laterally continuous	2.48	0.85	5.1	9.4	35.8	34.5	0.0	6.8	4.7	3.8

Table 2 (continued)

Deposit name	Thickness (cm)	Colour	Lithofacies type: lithology and sedimentary structure	GSD		Componentry $\geq 2$ mm (wt%)							
				$\sigma\phi$	Md	HVP	MVP	LVC	DDC	C	Ox	Alt	B
E2-I	3	Beige	Type II: framework-supported, uncompacted angular lapilli, massive, layer thickness is laterally continuous	1.88	3.10	50.6	15.5	13.9	15.7	0.4	2.2	0.1	1.5
E2-H	70	Dark grey	Type III: uncompacted angular blocks and lapilli supported in an ash matrix, massive, layer thickness varies slightly at outcrop level	1.97	4.00	7.8	10.1	7.1	64.4	0.2	4.6	3.1	2.8
E2-G	160	Beige, turns red upwards	Type III: uncompacted rounded blocks and lapilli supported in an ash matrix, subordinate normal-graded lithics, diffuse-bedded, gradational lower contact, layer thickness varies significantly at outcrop level	3.53	0.72	73.0	16.4	2.0	5.1	0.7	1.5	0.1	1.2
E1-F fine	3 layers, 3 cm each	Grey to brown	Type I: uncompacted coarse and fine ash, massive, laterally continuous intercalated parallel-bedded with E1-G coarse	3.46	0.70	3.8	19.1	42.6	26.0	1.3	2.6	1.5	3.1
E1-F coarse	3 layers, 2 cm each	Grey	Type I: framework-supported, uncompacted angular lapilli and coarse ash, subtle normal grading, laterally continuous intercalated parallel-bedded with E1-G fine	1.57	0.95	44.7	6.1	8.8	29.4	2.4	1.7	3.0	3.9
E1-E	22	Light grey	Type I: framework-supported, uncompacted angular lapilli and ash, marked inverse grading, layer thickness is laterally continuous	3.05	0.72	35.6	13.8	9.7	33.7	0.6	1.0	1.7	4.0
E1-D fine	2 layers, 4 cm each	Dark grey	Type I: uncompacted coarse and fine ash, massive, intercalated laterally continuous parallel-bedded with E1-E coarse	2.43	0.43	0.0	8.6	42.6	40.0	0.2	2.3	2.9	3.5
E1-D coarse	2 layers, 3 cm each	dark grey	Type II: framework-supported uncompacted angular lapilli and coarse ash, subtle normal grading, intercalated laterally continuous parallel-bedded with E1-E fine	1.57	1.30	3.1	6.0	43.7	35.2	1.6	0.3	8.7	1.4
E1-C	5	Beige	Type II: framework-supported uncompacted rounded lapilli, massive, layer thickness is laterally continuous	2.38	11.00	41.6	10.8	42.6	1.3	0.1	0.9	2.2	0.5
E1-B	70	Beige	Type II: framework-supported, uncompacted angular blocks, lapilli and ash, marked normal grading, layer thickness is laterally continuous	2.35	2.00	65.7	16.2	1.2	5.8	0.3	1.3	1.9	7.6
E1-A	10	Dark grey	Type I: uncompacted coarse and fine ash, laterally continuous subtle parallel layering	1.66	0.32	9.2	5.1	0.0	66.2	0.0	12.4	5.0	2.1



### Componentry and cumulative grain size distribution (GSD)

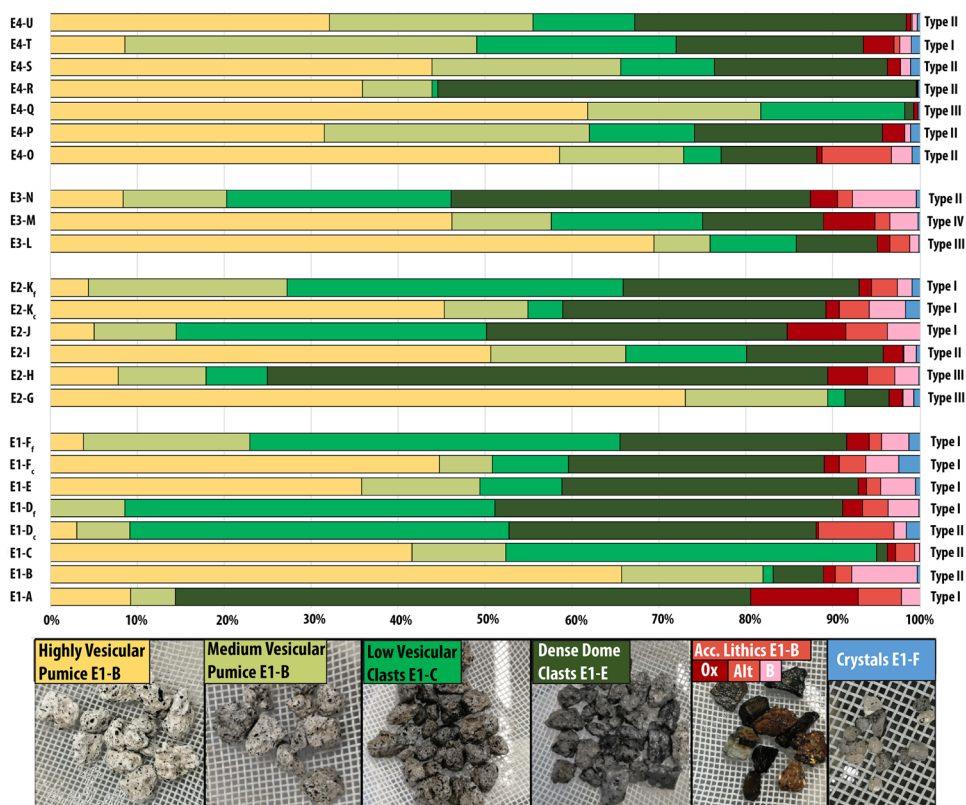
As apparent in Table 2 and illustrated in Fig. 3, proportions of juvenile material (i.e. highly vesicular pumice HVP, medium vesicular pumice MVP, low vesicular clasts LVC, dense dome clasts DDC and free crystals C) and accidentally incorporated older lithics (oxidised Ox, hydrothermally altered Alt and basement B material) vary strongly between deposits throughout all four episodes. Samples E1-B, E2-G, E3-L, and E4-Q have the highest pumice content (i.e. HVP and MVP), while samples E1-A, E1-D<sub>c+f</sub>, E1-F<sub>f</sub>, E2-H, E2-J, E2-K<sub>f</sub>, E3-N, and E4-R are the richest in low vesicular and dense clasts (i.e. LVC and DDC; see Fig. 2 for sample locations). The other eleven samples show similar amounts of vesicular and relatively dense clasts. Importantly, accidental clast content is especially high in the first deposit of Unit III (E1-A) (Table 2 and Fig. 3). Note that crystal content is low in all samples, as componentry was performed on grains larger than 2 mm in diameter.

Cumulative grain size distributions and total pumice (HVP + MVP) content of the 24 analysed samples are depicted in Fig. 4 and show that this proximal outcrop preserves deposits that range from fine- to coarse-grained, are poorly to moderately well-sorted, and are pumice-rich to pumice-poor. Figure 4a shows the cumulative GSD curves

of the nine samples that correspond to the lithofacies Type I, i.e. laterally continuous mainly coarse and fine ash deposits with a median grain size smaller than 1 mm (Md  $\phi < 1$  mm, Table 2). Most of these samples were taken from throughout E1 and from high in the E2 sequence; they also include five samples from three cycles of alternatingly coarser- and finer-grained deposits (Fig. 2). The finest-grained deposit is E2-J, a poorly sorted ( $\sigma\phi = 2.5$ ) deposit rich in dense dome-rock and accidental clasts (LVC, DDC and Acc, respectively, in Table 2 and Fig. 3) that was emplaced close to the end of E2 (Fig. 2). On the coarser end, the cumulative GSD curve of sample E1-E stands out because of its two modes at  $-2\phi$  (4 mm) and  $1\phi$  (0.5 mm). E1-E is an HVP- and DDC-rich deposit (Fig. 3) with marked inverse grading and consequent poor overall sorting ( $\sigma\phi = 3.1$ , Table 2 and Fig. 2). Samples E1-F<sub>c</sub> and (to a lesser degree) E1-K<sub>c</sub> are coarser-grained layers of alternating deposits (Fig. 2) and are distinguished because of their moderately good sorting ( $\sigma\phi = 1.7$ ) and relatively low fines content. Finer-grained layers of the alternating deposits E1-D<sub>f</sub>, E1-F<sub>f</sub> and E1-K<sub>f</sub> are characterised by a secondary mode in their fine ash fraction (8–6  $\phi$  or 0.0156 to 0.0039 mm, Fig. 4a), their consequent poor sorting ( $\sigma\phi = 2.4$ –3.5, Table 2) and their relatively low pumice content (Fig. 3).

Figure 4b shows the cumulative GSD curves of the ten samples that correspond to lithofacies Type II, i.e.

**Fig. 3** Componentry of the 24 sampled deposits of Unit III in stratigraphic order (youngest on top) for combined size fractions  $-7$  to  $-1\phi$ . The subscripts c and f denote samples of coarser- and finer-grained layers of cyclic alternating deposits. Component types and colour legend are shown below. Types refer to the lithofacies types described in Table 1



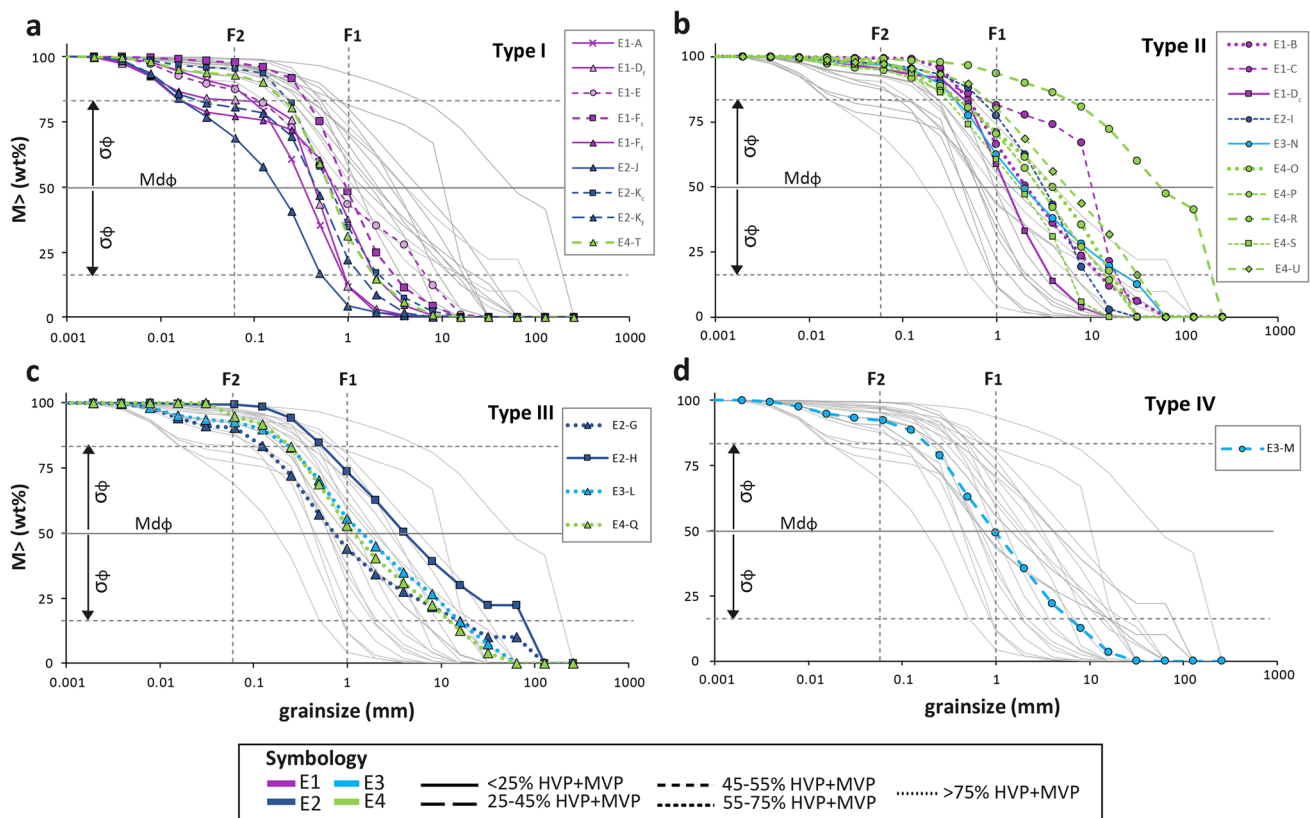


**Fig. 4** Cumulative grain size distributions of (a) nine Type I, (b) ten Type II, (c) four Type III and (d) one Type IV deposits. Samples are classified by eruptive episode (E1 to E4) and pumice (HVP+MVP) content. Grey solid line at 50% indicates the median ( $Md\phi$ ) and

dashed lines at 16 and 84% the standard deviation ( $\sigma\phi$ ). F1 (1 mm) and F2 (63  $\mu\text{m}$ ) plotted as reference for fine and very fine ash, respectively

framework-supported, laterally continuous mainly (block and) lapilli deposits ( $Md\phi > 1\text{ mm}$ , Table 2). In the field, these deposits range from thick ( $> 70\text{ cm}$ ) to thin ( $< 5\text{ cm}$ ), are moderately well ( $\sigma\phi = 1.5$ ) to poorly ( $\sigma\phi = 3.0$ ) sorted and appear throughout E1 to E4 (Table 2 and Fig. 2). On the fine-grained end is the pumice-poor sample E1-D<sub>c</sub>, which appears in alternation with an even finer-grained Type I deposit of similar componentry (Figs. 2 and 3). At the other extreme, sample E4-R stands out because of its high number of DDC blocks ( $Md\phi = 57\text{ mm}$ ) embedded in finer pumiceous material (Table 2). E1-C, an HVP- and LVC-rich sample, catches the eye because of its narrow cumulative GSD curve, which reflects its prominent mode at  $-3\phi$  (8 mm). The other eight deposits of this type lie in the middle of this grain size range, regardless of their pumice content (HVP+MVP = 20–80%, Table 2 and Fig. 3); grain size variations reflect the amount of incorporated lapilli  $> 10\text{ mm}$  in diameter (Fig. 4b).

As can be seen in Fig. 4c, out of the four cumulative GSD curves of the lithofacies Type III samples (i.e. matrix-supported, diffusely stratified, blocks, lapilli and ash deposits with laterally varying thickness), the three pumice-rich

samples E2-G, E3-L and E4-Q have similarly gentle slopes that indicate poor sorting ( $\sigma\phi = 2.9\text{--}3.5$ ; Table 2). Sorting is better for the dense-dome-clast-rich E2-H sample ( $\sigma\phi = 1.97$ ), which has relatively little fine-grained material. Finally, E3-M, the only sampled Type IV deposit (i.e. matrix-supported, laterally discontinuous thin-bedded subparallel and cross-stratification, lapilli and ash deposit) also shows a gentle cumulative GSD curve ( $\sigma\phi = 2.5$ ) while incorporating fewer clasts  $> 10\text{ mm}$  when compared to Type III samples (Fig. 4d).

## Petrography

Petrographic analysis of 16 representative juvenile pyroclasts (i.e. four per episode and juvenile clast category) shows a phenocryst assemblage of plagioclase, hornblende, oxides and apatite (see also Andrade et al. 2021). Vesicularity of the analysed clasts ranges from 3% in DDC to 70% in HVP clasts (Fig. 5a). Although bulk crystallinity decreases from 32 to 8% with increasing vesicularity (Fig. 5b), melt crystallinity ( $100 \cdot \text{bulk crystallinity} / [1 - \text{vesicularity}]$ ) is relatively constant across all episodes and most vesicularities

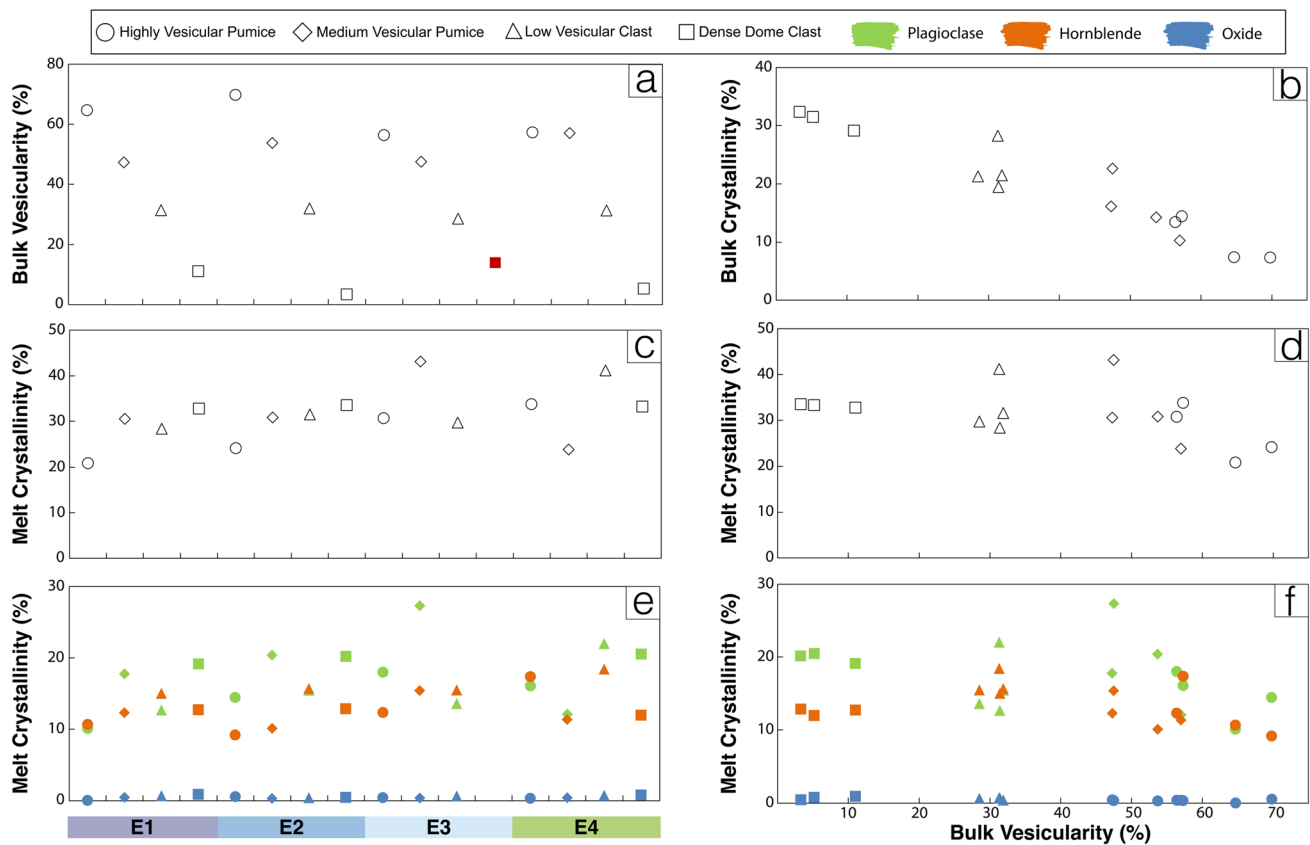


**Fig. 5** Vesicularity and crystallinity analyses of 16 clasts: four per episode (E1–E4) and juvenile component type (HVP, MVP, LVC and DDC). Bulk vesicularity (a) and crystallinity (b) are area fractions of the entire clast; melt crystallinity (c, d) is bulk crystallinity/

(1 – vesicularity). (e, f) Mineral assemblage as plagioclase, hornblende and oxide (oxides + apatite). Red E3-DDC clast is a brecciated lithic that was not analysed

(Fig. 5c, d). Melt crystallinity decreases slightly at a bulk vesicularity of ~56% (HVP samples), a change that reflects variations in plagioclase content (10–27% overall); hornblende crystallinity remains constant at 10–16% throughout (Fig. 5e, f). SEM images of phenocryst macrotextures can be found in ESM-2.

Phenocryst size distributions show no obvious change with eruptive episode (Fig. 6). Across the entire crystal population, the median size ( $M_{dx}$ ) ranges from 0.57 to 1.45 mm (Fig. 6a). By phase, plagioclase crystals are more variable and larger ( $M_{dx}$  = 0.66–2.2 mm; Fig. 6b) than hornblendes ( $M_{dx}$  = 0.45–0.8 mm; Fig. 6c). Both crystal phases have occasional large (> 1 mm; plagioclase 2–5 mm) crystals that contribute to observed variations in melt crystallinity (Fig. 5e, f). The most pronounced variation in median crystal size is between the different end member component types DDC and HVP, with DDC having slightly larger median hornblende sizes and substantially larger plagioclase crystals than highly vesicular pumice clasts (Fig. 6d); plagioclase sizes in MVP and LVC clasts are variable.

All analysed DDC have hornblende phenocrysts with thick reaction rims and varying amounts of a groundmass Si-phase (likely vapour-phase cristobalite; Fig. 7a, c; Horwell et al. 2013). In contrast, HVP clasts in all samples have microlite-free groundmass glass (Fig. 7d) and phenocrysts of plagioclase and amphibole that are euhedral and lack reaction rims, although individual crystals are commonly broken. The E4-U LVC also has a thick breakdown rim; LVCs in E1 (C) and E3 (N) have thin reaction rims and groundmass cristobalite. The E4-U MVP clast has a mixed hornblende population that contains crystals both with and without breakdown rims. MVP clasts in E2–E4 also have well developed plagioclase microphenocryst populations (Fig. 7b). Qualitatively, the sizes and number of vesicles varies among clasts, but all samples lack large vesicles (Fig. 7; ESM-2).

### Phase textures and compositions

An exploratory analysis of plagioclase and amphibole phenocryst textures and compositions shows that

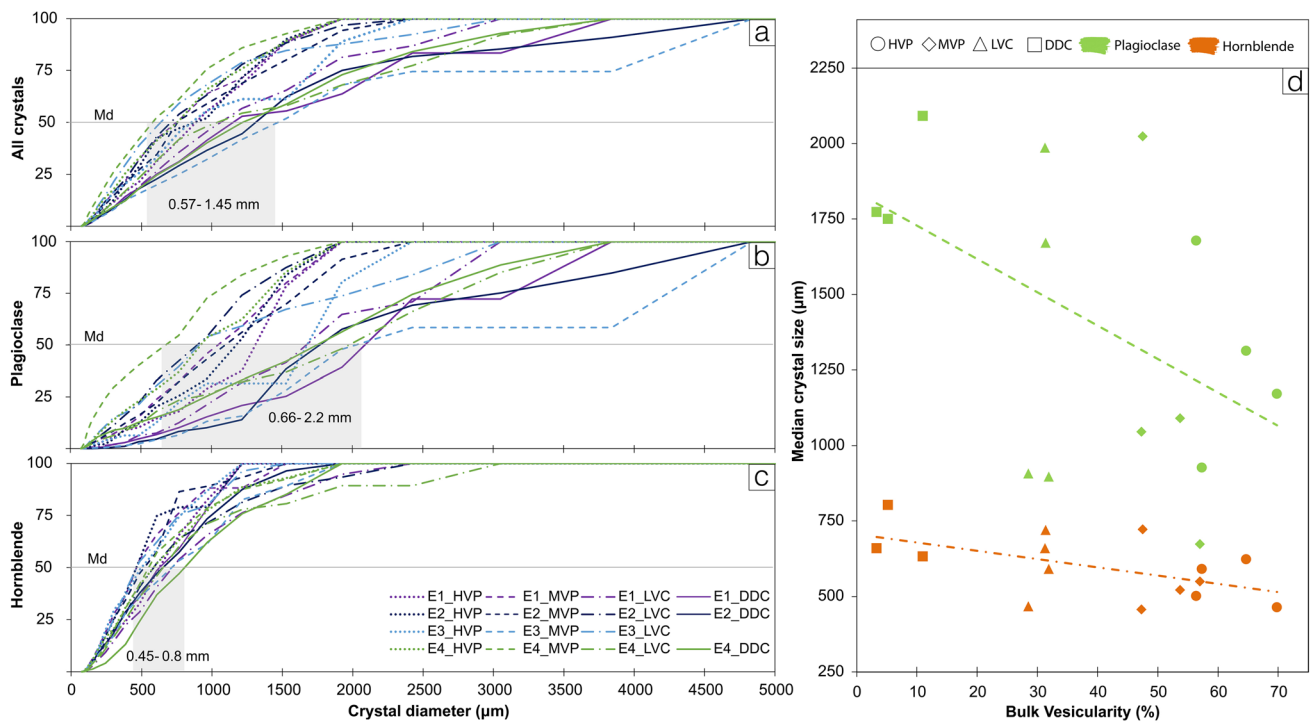


**Fig. 6** (a–c) Crystal size distributions as cumulative distribution functions (CDFs) from 15 clasts (excluding lithic E3-DDC) for (a) all crystals, (b) plagioclase and (c) hornblende. Grey square indicates

median size range. (d) Median crystal size against bulk vesicularity for plagioclase and hornblende. Dotted lines are visual trends

**Fig. 7** Back-scattered electron (BSE) images of representative microtextures, labelled by stratigraphic layer and component type. All images at 250× magnification (see 100 μm scale bar in (d)). Vesicles are black, glass is grey and brightness increases for crystal phases Si-phase, plagioclase, amphibole and Fe-Ti oxide

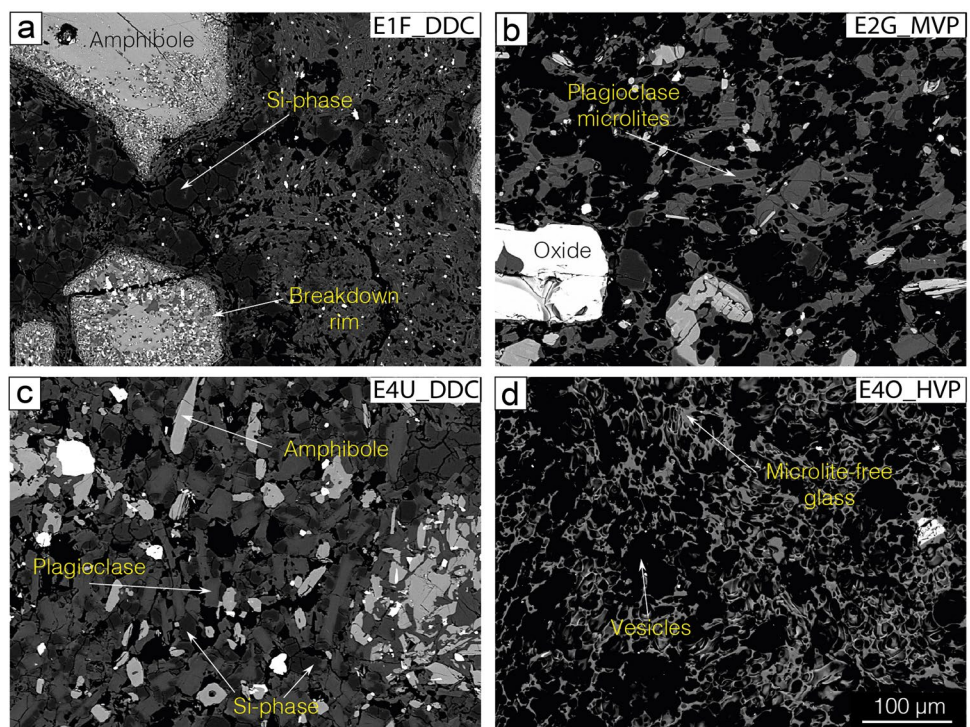
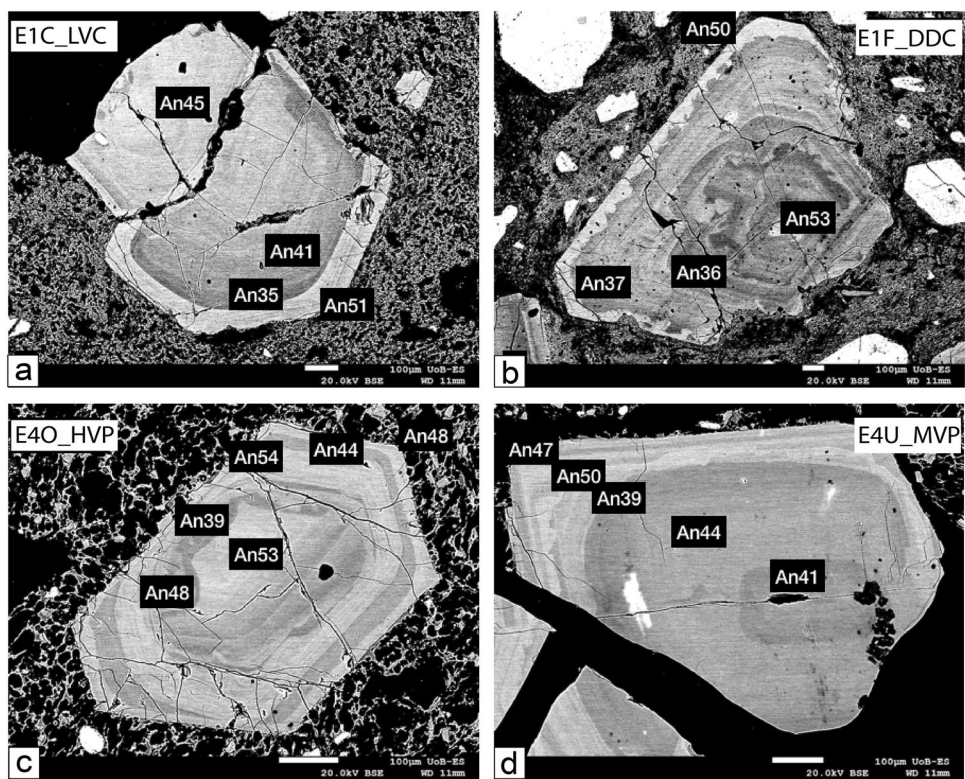


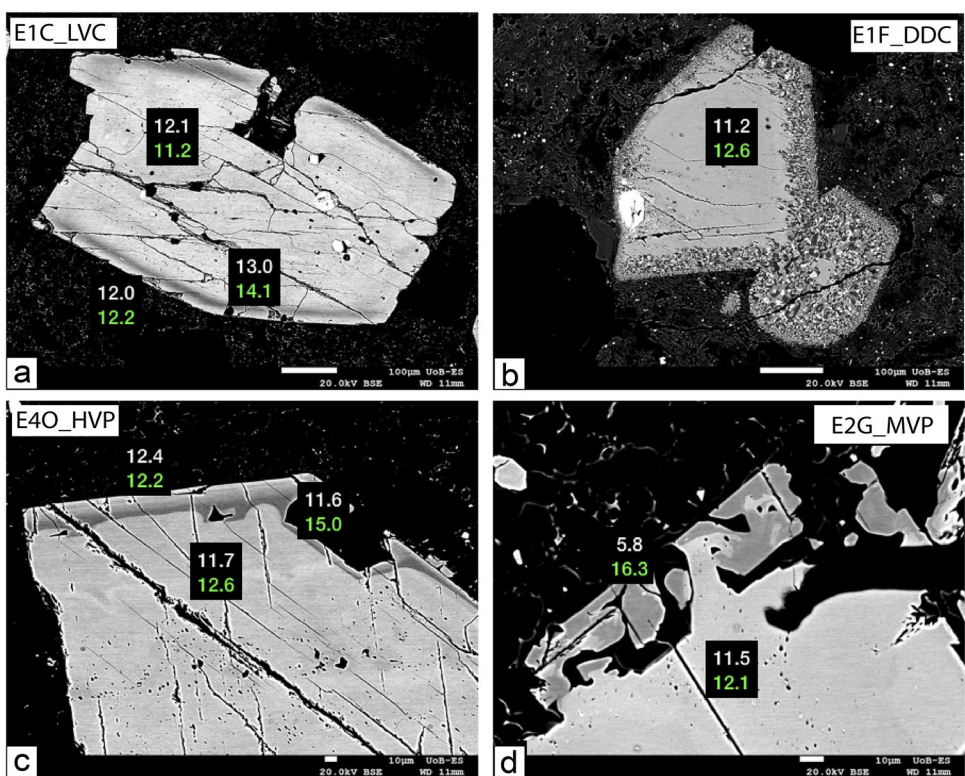
**Fig. 8** Examples of plagioclase textures and compositions from E1 and E4 deposits. Compositions shown by anorthite content (An). (a, b) Typical plagioclase phenocrysts from E1; note pronounced anorthitic rims. (c, d) Typical plagioclase phenocrysts from E4; An-rich rims have more complex oscillatory zoning than in E1. Scale bars are 100  $\mu$ m



plagioclase phenocrysts display extensive oscillatory zoning within crystal cores, mantles and rims (Fig. 8). Plagioclase crystal cores commonly have rounded margins,

may include internal resorption zones and typically preserve substantial proportions of albitic (An<sub>35–45</sub>) in addition to more anorthitic ( $\leq$  An<sub>53</sub>) compositions. Crystal

**Fig. 9** Example amphibole textures and compositions labelled by stratigraphic layer and component type. Compositions shown by wt% Al<sub>2</sub>O<sub>3</sub> (white) and wt% MgO (green). (a) Amphibole with pronounced high Al<sub>2</sub>O<sub>3</sub> high MgO inner rim. (b) Core surrounded by coarse-grained breakdown rim. (c) High Al<sub>2</sub>O<sub>3</sub> high MgO inner rim in E4 HVP crystal overgrows pronounced resorbed margin. (d) Late-stage low Al<sub>2</sub>O<sub>3</sub> and very high MgO overgrowth rim. Scale bars are 100  $\mu$ m in (a, b) and 10  $\mu$ m in (c, d)



rims have near-uniform compositions of  $An_{47-51}$  (Fig. 8) that contrast with typical mantle compositions of  $An_{35-44}$ . The outer mantle zones are either rounded (Fig. 7a, c, d) or strongly resorbed (Fig. 7b); rims are euhedral and zoned. Rims in E4 crystals are also notable in having relatively high FeO (> 0.4 wt.%; ESM-2).

Amphibole phenocrysts also vary in composition (shown in Fig. 9 as variations in  $Al_2O_3$  [white numbers] and MgO [green numbers]), although most are classified as tschermakitic pargasite (ESM-2). There is faint evidence of internal zoning, commonly with a mottled appearance (Fig. 9c, d). Many phenocrysts show a thin but abrupt and pervasive high MgO inner rim (dark zones in Fig. 9a, c). Late-stage skeletal overgrowths (Fig. 9d) are common in E4-Q and E2-G; these have low  $Al_2O_3$  (7.5 wt%) and high MgO (> 15 wt%) and are classified as Mg-hornblende. Breakdown rims, where evident, often show grain size variations in the breakdown products from fine-grained rims to coarser-grained interiors; the latter may penetrate finger-like into the crystal core (Fig. 7a).

## Discussion

First, we discuss the limitations of this investigation regarding the selection of the outcrop and the number of laboratory-analysed clasts. Then we combine lithofacies description, grain size (GSD) and componentry data to assess deposit type and formation and explore the origin of the various clast types using textural and petrologic observations. Finally, we propose an eruptive sequence for Unit III.

### Potential limitations of our analysis

We start by reviewing potential limitations of this investigation, including (i) only a single outcrop was studied in detail, and (ii) only representative pyroclasts were scrutinised in the laboratory. As explained above, this single outcrop was selected out of the tens of outcrops visited, including the seven sections studied in detail by Andrade et al. (2021), because it best exposes the full pyroclastic sequence of Unit III. Importantly, detailed characterisation of one or two proximal sections is a common strategy for describing complex eruptive sequences (Houghton et al. 2004; Gurioli et al. 2005; Carey et al. 2007). In this context, this first thorough characterisation of the Pudahua stratigraphy provides a framework for detailed analysis of individual deposits or deposit packages and associated eruptive styles, including determination of layer volumes, footprints of ash fall and total grain size distributions.

The second limitation arose from reduced access to laboratories during the COVID-19 pandemic, which forced us to perform componentry analysis in an improvised home-lab.

This environment, however, prompted us to develop a relative clast density classification scheme, which can be performed independently of laboratory access, including in the field. While only semi-quantitative, our relative density scheme allowed us to discriminate between highly vesicular, medium vesicular, low vesicular and dense clasts, which, in combination with other clast characteristics like colour, shape and crystallinity, is useful for juvenile component distinction. Additionally, this method presents the opportunity to assess relative densities of clasts > 2 mm, while the standard paraffin method is usually only applied on clasts > 8 mm. Moreover, since on average 300 clasts were analysed per sample fraction > 2 mm for each of the 24 samples, tens of thousands of clasts were scrutinised in this manner, which would have been impossible if we had followed the standardised density assessment method. Finally, our relative classification of clast densities/vesicularities was later verified by the application of the standardised paraffin method on four clasts of each class (see the “Petrographic and textural analysis” section).

### Indicators of deposit origin and eruptive style

We follow Branney and Kokelaar (2002) in using granulometry, stratification, grading and bedding to categorise deposits corresponding to lithofacies Type I as fine to coarse ash fall and Type II as lapilli (and block) fall; deposits displaying lithofacies Types III and IV are interpreted to be pyroclastic current deposits, with the former corresponding to granular fluid-based and the latter to fully dilute currents. The densely indurated, coarse-ash and porous matrix of the lithofacies Type V deposit indicates that it is reworked and most likely a debris flow. In all cases, componentry may vary from pumice- to lithic-rich, offering further insights into the eruptive styles that accompanied deposit formation. Based on the presented data, we interpret the 24 sampled deposits as:

- Ash fall sample *E1-A*, characterised by a fine-grained and relatively well sorted GSD, laterally continuous subtle parallel layering and a high accidental (20%) and dense (66%) clast and subordinate pumice (14%) content (Figs. 3, 4a), fits the description of *hydromagmatic* fall deposits (Heiken and Wohletz 1987; Villemant et al. 1996; Miyabuchi et al. 2013), which agrees with the interpretation by Papale and Rosi (1993) for this deposit.
- The abundant highly vesicular ( $\geq 65\%$ ) and total (HVP + MVP  $\geq 80\%$ ) pumice content of lapilli and block fall sample *E1-B* attests to the rapid ascent of deep-seated volatile-rich magma (Carazzo et al. 2012; Cioni et al. 2015; Maeno et al. 2019). This, in addition to the significant thickness ( $\geq 70$  cm) of the deposits at this close proximity to the crater, indicates that these deposits were most likely formed by *Plinian-type* eruptions, as purported by

Papale and Rosi (1993), who estimated E1-B to be at the lower end of a VEI 4. Pyroclastic current deposits *E2-G*, *E3-L*, and *E4-Q* (Figs. 2, 3 and Table 2) have similar component characteristics to E1-B, but different sedimentary structures, and are categorised as ignimbrites.

- Massive pumice lapilli fall deposits *E4-O* and *E4-P*, while thinner, also have a high ( $\geq 62\%$ ) total pumice content and precede thick massive to diffusely stratified pumice-rich pyroclastic current deposits (or ignimbrites) (Figs. 2, 3). We suggest that these fall deposits may represent the early sustained phase of *Plinian-type* eruptive columns that then collapsed to form pyroclastic currents.
- Lapilli fall samples *E1-C*, *E1-E*, *E2-I*, and *E4-U* are distinguished by their lower HVP ( $\leq 50\%$ ) and higher LVC + DDC (29–43%) proportions (Fig. 3, Table 2). The wider density range of the juvenile clasts suggests a *Sub-Plinian* origin (Cashman 2004; Sulpizio et al. 2007; Castruccio et al. 2016).
- The wide density range of juvenile clasts in alternatingly finer- and coarser-grained ash fall samples *E1-D*, *E1-F* and *E2-K* (Figs. 2, 3 and Table 2) match descriptions of *Vulcanian* ash fall deposits (Bonadonna et al. 2002; Cashman 2004; Komorowski et al. 2010). These deposits probably formed accompanying dome-growth episodes (Heiken and Wohletz 1987). In general, higher pumice content (e.g. E1-F and E2-K; Fig. 3) suggests faster dome growth, more efficient conduit evacuation and shorter repose intervals (Druitt et al. 2002; Wright et al. 2007).
- Finally, elevated accidental clast and/or dense dome clast proportions, as observed in samples *E2-H*, *E2-J*, *E3-M*, *E3-N* and *E4-R*, have been associated with *vent migration*, *widening* or *opening of new vents* that caused (partial) destruction of co-eruptive and/or older domes (Turbeville et al. 1989; Lavallée et al. 2012; Maeno et al. 2019).

### Textural and petrologic evidence for the origin of different clast types

Clast textures and phenocryst compositions record conditions of magma storage prior to and during the Unit III eruptions. The wide but consistent range in phenocryst compositions and median size for all analysed pyroclasts (Figs. 6, 8, 9; ESM-2) suggests entrainment of crystals from a similar depth range throughout the entire eruptive sequence. For example, compositionally based estimates of pressure and temperature using the calibration of Ridolfi and Renzulli (2012), although approximate, suggest equilibration of amphibole cores and mantles in these samples at 250–450 MPa and  $\sim 890$  °C. All eruptive units also show relatively high-An plagioclase rims overgrown on resorbed lower An mantles. This pattern is most easily explained by individual eruptions within the sequence involving transport of previously stored crystals within a hotter/less

evolved melt. Similarly, we interpret the dark (high MgO, Al<sub>2</sub>O<sub>3</sub>) outer rims in E1 (Fig. 9a) and E2, which yield unrealistically high pressures ( $> 500$  MPa) using the simple amphibole thermobarometer of Ridolfi and Renzulli (2012), to reflect an abrupt increase in melt temperature and change in melt composition, indicating injection of a hotter magma into the dacitic reservoir (Manrique et al. 2020). That these features appear in all eruptive episodes suggests that the Unit III activity was driven by persistent magma recharge into the Pululahu system.

Additional information about pre- and inter-eruptive magma storage and ascent comes from textural features evident in microtextural images (Cashman and McConnell 2005; Browne et al. 2006). Notably, HVP, MVP and LVC samples from E1 (B and C) and HVP sample E2-G have vesicular, microlite-free glass, lack hornblende breakdown rims, and generally show little evidence of shallow pre-eruptive storage. These characteristics indicate rapid magma transfer from depth to the surface, consistent with the rapid onset of main-phase Plinian-type Unit III activity. HVP samples from E3-N and E4-O (sub-) Plinian eruptions have unreacted amphibole but well-developed plagioclase microphenocrysts that record magma tapped from below the location of hornblende breakdown but above the level of H<sub>2</sub>O saturation and an associated second stage of plagioclase crystallisation. This observation suggests that by E3 time, an intermediate-level magma storage system had developed, as seen at Mount St. Helens, WA, during dome-growth phases of the eruption (Cashman and McConnell 2005). Mixed amphibole populations (with and without breakdown rims) in MVP samples from the Plinian-type deposit E2-G and sub-Plinian deposit E4-U also suggest eruptive magma drawdown over a range that crossed the hornblende stability field, again similar to dome-building phases of the Mount St. Helens eruption. Late-stage overgrowths on amphibole in these samples (Fig. 9c, d) yield the lowest amphiboles temperatures ( $< 850$  °C) and pressures ( $< 200$  MPa) (ESM-2).

Finally, the thick and often coarse-grained amphibole breakdown rims evident in all DDC samples (E1-F, E2-H, E3-N, E4-U) and LVC E4-U (Figs. 7a, 9b) indicate shallow magma storage ( $< \sim 75$  MPa) that, together with the high FeO in plagioclase rims of E4 samples, provides evidence of shallow pre-eruptive cooling and crystallisation. Late-stage crystallisation at shallow levels is also evidenced by the increase in plagioclase size in DDC clasts (Fig. 6d; Riker et al. 2015) and the presence of a groundmass Si-phase (Fig. 7a; Horwell et al. 2013; Schipper et al. 2015). Since these clasts come from very different deposit types, we infer that all eruptions except the most vigorous Plinian-type phases, regardless of their dynamics, incorporated shallowly stored and efficiently degassed magma. The thin and fine-grained breakdown rims and groundmass Si-phase in LVC

(E2-I and E3-N) samples, in contrast, indicate very shallow storage in a conduit plug or cryptodome (Fig. 7; ESM-2) which agrees with the interpretation of (partial) dome destruction during sub-Plinian eruptions.

### Eruptive style transitions and sequence of events at Pululahua

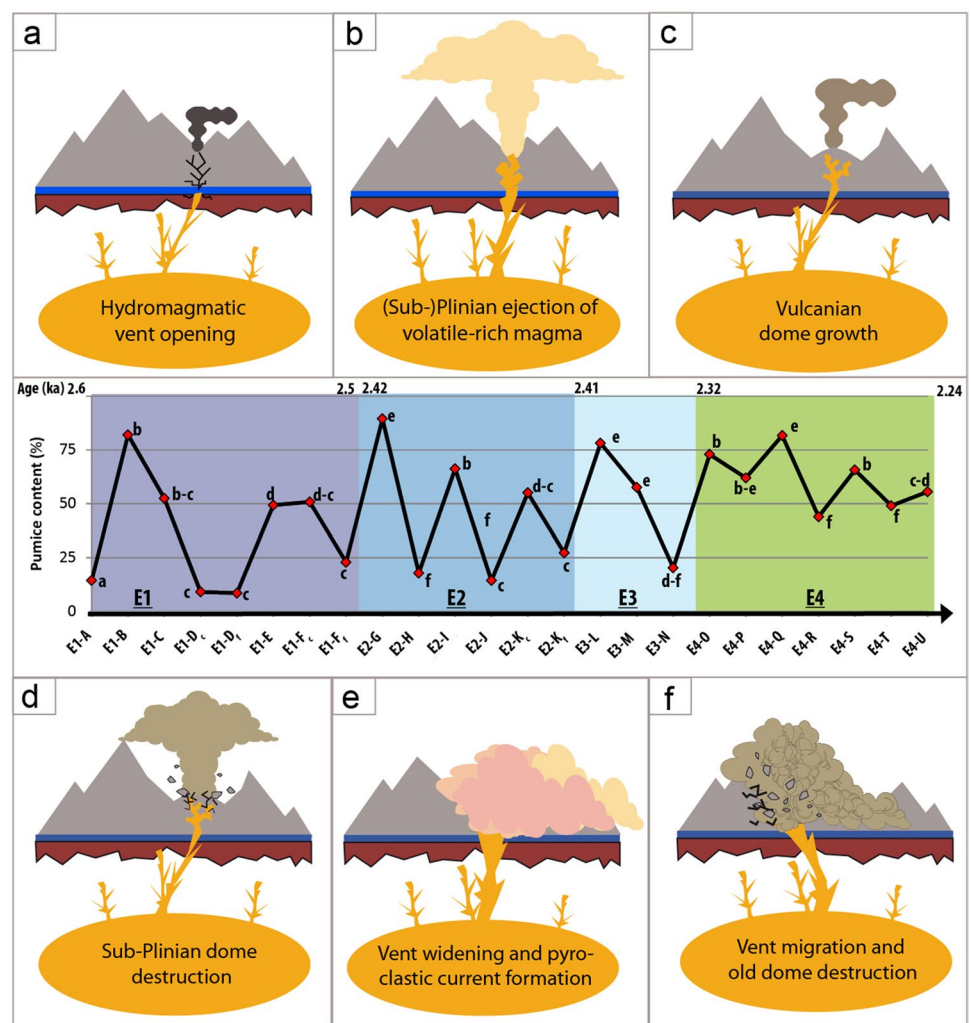
Here we use our field observations, GSD trends, compositional proportions, pyroclast analyses and the current morphology of Pululahua to construct an eruptive history for Pululahua from ~2.6 to ~2.3 ka (Fig. 10).

The explosive sequence initiated with discrete hydro-magmatic pulses triggered by ascending magma that came into contact with groundwater and opened the first vent (E1-A, Fig. 10a, see also Papale and Rosi 1993). The resulting sudden depressurisation of a deeper, volatile-rich magma drove the first, and largest, Plinian-type eruption (E1-B, Fig. 10b). Slower ascent following the release of accumulated pressure allowed partial pre-eruptive

degassing (E1-C). Even slower subsequent magma ascent and associated degassing caused episodic lava dome growth accompanied by Vulcanian explosions (E1-D, Fig. 10c). The new (degassed) lava dome acted as a plug for the underlying magmatic system and hindered volatile escape from below, allowing pressure build-up and a sub-Plinian eruption that destroyed the newly formed dome (E1-E, Fig. 10d). Renewed, but faster, dome growth with Vulcanian eruptions (E1-F) culminated with another sub-Plinian eruption that destroyed the second dome, forming the fall and flow deposits observed at the end of E1 (Fig. 2).

Revegetation after the first eruptive episode is preserved as charcoal at the base of a dilute pyroclastic current deposit that started E2. Progressive vent widening with each eruption produced large pumice-rich pyroclastic currents manifested as the ignimbrite of E2-G (Fig. 10e). Migration of the vent towards older domes caused their (partial) destruction and the formation of lithic-rich pyroclastic currents (E2-H, Fig. 10f). The lithostatic load

**Fig. 10** Graph illustrating the change in pumice (HVP + MVP) content observed in 24 pyroclastic deposit samples of Pululahua from the oldest to the youngest and their corresponding eruptive dynamism (a–f). Ages in ka from Andrade et al. (2021). Dark red layer represents basement rocks and blue layer indicates groundwater table





reduction resulting from dome destruction depressurised the underlying magmatic system and triggered another sub-Plinian eruption (E2-I). The end of E2 is marked by a new vent opening (E2-J) that terminated in a third dome growth episode (E2-K).

After a second break in activity, the base surge of the first pumice-rich pyroclastic current of E3 (ignimbrite E3-L) turned the marginally regrown vegetation into a fine-grained charcoal layer. This granular fluid-based current and succeeding fully dilute ones (E3-M) further eroded the already wide vent. E3 ended with growth of a fourth dome that was shattered by two more sub-Plinian eruptions (E3-N), whose explosive power further damaged the old domes.

A Plinian-type eruption incorporated charred vegetation particles as it initiated the last explosive episode of Unit III (E4-O). Collapse of the Plinian column generated a pumice-rich pyroclastic current with base surges; a second Plinian-type eruption (E4-P) assimilated remnants of the youngest dome and formed another pumice-rich pyroclastic current (ignimbrite E4-Q). By that time, Pululahua's crater was sufficiently deep to retain pyroclastic material within the crater walls and clog the vent. A violent sub-Plinian eruption then opened a new vent close to the older domes, causing their destruction and incorporating block-sized dense dacites in the ensuing fall deposit (E4-R, E4-S and E4-T), which was followed by additional pyroclastic currents. A short break in activity preceded a smaller and two larger sub-Plinian eruptions that accompanied the semi-explosive growth of the final intra-depression domes (E4-U, Fig. 10). This activity marked the gradual transition of Unit III into effusive Unit IV dated at 2.24 ka (Andrade et al. 2021).

In summary, our analysis agrees with that of Andrade et al. (2021) that a caldera collapse origin of the Pululahua depression can be excluded. First and foremost, the full DRE volume for Unit III of  $0.58 \pm 0.25 \text{ km}^3$  is too small to create the observed depression; additionally, it must be further divided into at least the four eruptive episodes separated by times of quiescence long enough for vegetation regrowth (approximately 300 years in total). Our detailed analysis of the Unit III deposits, in contrast, paints a picture of a period of intermittent explosive and effusive activity that was probably fuelled by an increase in the rate of magma supply to the sub-volcanic system. We note that future studies that include more detailed physical and petrological analysis could solidify our interpretations of the multiple events that comprise Unit III, while diffusion chronometry of phenocrysts could better constrain time breaks and recharge rates within the Pululahua system. Future microtextural work on targeted clasts could additionally constrain shallow conduit dynamics and eruptive transitions by analysing pore space connectivity, and the size distributions and number densities of microlites and vesicles. Coupled with more petrological analysis throughout the Unit III sequence, this work would not only provide a detailed window into

the Pululahua magmatic plumbing system but also improve analysis of potential future eruptions of this volcano.

## Conclusion

Detailed inspection of 70 pyroclastic deposits that comprise the explosive sequence of Pululahua between 2.6 and 2.3 ka shows that these 300 years of eruptive activity were characterised by numerous transitions between *effusive* and *explosive* activity and repose periods. The pulsating nature of the eruptions produced phases with dominant fall or flow influence, with fall deposits dominating primarily in the early stages of Unit III. High-An plagioclase rims observed throughout the explosive sequence suggest that Unit III activity was ultimately driven by episodic magma recharge into the Pululahua system. After the explosive period was initiated by hydromagmatic activity and a VEI 4 Plinian-type eruption, juvenile material with a wide density range and characteristic amphibole breakdown rims indicate Vulcanian activity accompanying emplacement of at least four ephemeral domes, which were later destroyed by sub-Plinian eruptions. The textural data provide evidence for eruption of magma from throughout the magma storage system in all eruptive episodes, but with increasing evidence for shallow pre-eruptive magma storage (including the conduit) and degassing in later-erupted episodes. Importantly, incorporation of older dacitic dome and basement material in many deposits records destruction of pre-existing domes and pre-Pululahua structures through vent widening and migration. Dome destruction, perhaps accompanied by syn-eruptive magma withdrawal, created a  $13 \text{ km}^2$ , 300-m-deep depression, and left behind two dome-conduit remnants to the southwest (El Chivo I and II). This finding revises the previous classification of the Pululahua depression as a caldera; instead, we suggest it is the morphological result of decades of intense explosive-effusive volcanic activity. Additional evidence for protracted formation of the depression comes from three breaks in Unit III activity that subdivide this explosive sequence into four episodes and that were long enough for vegetation regrowth (charcoal-rich layers). Finally, we note that Pululahua has the potential of future activity involving numerous Plinian-type and sub-Plinian eruptions over a long time period that may be separated by phases of effusive dome-growth and repose. It is the unforeseeable transitions in eruptive styles that pose the largest risk to the nearby population. However, it should be noted that highly explosive eruptions took place during only 300 of more than 18,000 years of eruptive volcanic activity at Pululahua, which is currently in a state of rest.

**Supplementary Information** The online version contains supplementary material available at <https://doi.org/10.1007/s00445-022-01590-4>.

**Acknowledgements** The authors thank the Instituto Geofísico, Escuela Politécnica Nacional (IG-EPN) for logistical support during fieldwork and laboratory analyses, as well as Marco Almeida and Astrid Müller for joining the field campaigns and sharing their ideas. A special acknowledgment goes to Stuart Kearns and Ben Buse, University of Bristol, who kept the SEM and EPMA running safely through the pandemic. Finally, the authors would like to thank Professor Daniel Andrade for being the first to question the classification of Pululahuá as a caldera and planting the seed for further studies on this volcanic complex. Ulrich Kueppers, Adriano Pimentel and an anonymous reviewer are kindly acknowledged for their thoughtful comments that improved the manuscript.

**Author contribution** AVM conceived of the project, conducted all analyses that were completed in Ecuador and wrote the main manuscript draft. KVC supervised the research and performed the petrologic analyses. SJM did the density measurements, SEM imaging and image analysis. FJV assisted during field work, GSD and componentry analysis, as well as deposit origin interpretation. All authors revised and enhanced the manuscript.

**Funding** KVC was funded by an AXA Research Professorship; FJV was funded by UKRI GCRF under grant NE/S009000/1, Tomorrow's Cities Hub.

## Declarations

**Conflict of interest** The authors declare no competing interests.

## References

- Adams NK, Houghton BF, Fagents SA, Hildreth W (2006) The transition from explosive to effusive eruptive regime: the example of the 1912 Novarupta eruption, Alaska. *Geol Soc Am Bull* 15
- Águila C (1986) Geovolcanología del complejo Pululahuá-Casitahuá y sus implicaciones geotérmicas. Unpubl. Diploma thesis, Universidad Central del Ecuador
- Almeida M (2016) Estudio Petrográfico y Geoquímico del Volcán Cotacachi, Provincia de Imbabura. Unpubl. Diploma thesis, Escuela Politécnica Nacional
- Andrade D, Vásconez Müller A, Vasconez FJ et al (2021) Pululahuá dome complex, Ecuador: eruptive history, total magma output and potential hazards. *J South Am Earth Sci* 106:103046. <https://doi.org/10.1016/j.jsames.2020.103046>
- Bonadonna C, Mayberry GC, Calder ES et al (2002) Tephra fallout in the eruption of Soufrière Hills Volcano, Montserrat. *Geol Soc Lond Mem* 21:483–516. <https://doi.org/10.1144/GSL.MEM.2002.021.01.22>
- Branney MJ, Kokelaar P (2002) Pyroclastic density currents and the sedimentation of ignimbrites. *Geol Soc Mem* 27:143
- Browne BL, Eichelberger JC, Patino LC et al (2006) Magma mingling as indicated by texture and Sr/Ba ratios of plagioclase phenocrysts from Unzen volcano, SW Japan. *J Volcanol Geotherm Res* 154:103–116
- Carazzo G, Tait S, Kaminski E, Gardner JE (2012) The recent Plinian explosive activity of Mt. Pelée volcano (Lesser Antilles): the P1 AD 1300 eruption. *Bull Volcanol* 74:2187–2203. <https://doi.org/10.1007/s00445-012-0655-4>
- Carey RJ, Houghton BF, Sable JE, Wilson CJN (2007) Contrasting grain size and componentry in complex proximal deposits of the 1886 Tarawera basaltic Plinian eruption. *Bull Volcanol* 69:903–926. <https://doi.org/10.1007/s00445-007-0117-6>
- Cashman K (2004) Volatile controls on magma ascent and eruption. In: Sparks RSJ, Hawkesworth CJ (eds) *Geophysical monograph series*. American Geophysical Union, Washington, D. C., pp 109–124
- Cashman K, McConnell SM (2005) Multiple levels of magma storage during the 1980 summer eruptions of Mount St. Helens. *WA Bull Volcanol* 68:57–75. <https://doi.org/10.1007/s00445-005-0422-x>
- Cassidy M, Manga M, Cashman K, Bachmann O (2018) Controls on explosive-effusive volcanic eruption styles. *Nat Commun* 9:2839. <https://doi.org/10.1038/s41467-018-05293-3>
- Castro JM, Gardner JE (2008) Did magma ascent rate control the explosive-effusive transition at the Inyo volcanic chain. *Calif Geol* 36:279. <https://doi.org/10.1130/G24453A.1>
- Castruccio A, Clavero J, Segura A, et al (2016) Eruptive parameters and dynamics of the April 2015 sub-Plinian eruptions of Calbuco volcano (southern Chile). *Bull Volcanol* 78:1007/s00445-016-1058-8. <https://doi.org/10.1007/s00445-016-1058-8>
- Christiansen RL, Peterson DW (1981) Chronology of the 1980 eruptive activity. *US Geol Surv Prof Pap* 1250:17–30
- Cioni R, Pistolesi M, Rosi M (2015) Plinian and Subplinian eruptions. In: Houghton B, McNutt S, Rymer H, Stix J (eds) *The encyclopedia of volcanoes*. Elsevier, pp 519–535
- Cole PD, Robertson REA, Fedele L, Scarpato C (2019) Explosive activity of the last 1000 years at La Soufrière, St Vincent, Lesser Antilles. *J Volcanol Geotherm Res* 371:86–100. <https://doi.org/10.1016/j.jvolgeores.2019.01.002>
- Druitt TH, Young SR, Baptie B et al (2002) Episodes of cyclic Vulcanian explosive activity with fountain collapse at Soufrière Hills Volcano, Montserrat. *Mem-Geol Soc Lond* 21:281–306
- Gardner CA, Neal CA, Waitt RB, Janda RJ (1994) Proximal pyroclastic deposits from the 1989–1990 eruption of Redoubt Volcano, Alaska — stratigraphy, distribution, and physical characteristics. *J Volcanol Geotherm Res* 62:213–250. [https://doi.org/10.1016/0377-0273\(94\)90035-3](https://doi.org/10.1016/0377-0273(94)90035-3)
- Giachetti T, Druitt TH, Burgisser A et al (2010) Bubble nucleation, growth and coalescence during the 1997 Vulcanian explosions of Soufrière Hills Volcano, Montserrat. *J Volcanol Geotherm Res* 193:215–231
- Global Volcanism Program, 2021. Report on Soufriere St. Vincent (Saint Vincent and the Grenadines) (Bennis, K.L., and Venzke, E., eds.). *Bulletin of the Global Volcanism Network*, 46:5. Smithsonian Institution. <https://doi.org/10.5479/si.GVP.BGVN202105-360150>
- Gurioli L, Houghton BF, Cashman KV, Cioni R (2005) Complex changes in eruption dynamics during the 79 AD eruption of Vesuvius. *Bull Volcanol* 67:144–159. <https://doi.org/10.1007/s00445-004-0368-4>
- Gutscher M-A, Malavieille J, Lallemand S, Collot J-Y (1999) Tectonic segmentation of the North Andean margin: impact of the Carnegie Ridge collision. *Earth Planet Sci Lett* 168:255–270
- Hall ML, Hillebrandt C (1988) Mapa de peligros volcánicos potenciales asociados con el volcán Pululahuá, Provincia de Pichincha (1:50000)
- Heiken G, Wohletz K (1987) Tephra deposits associated with silicic domes and lava flows. In: *Geological Society of America Special Papers*. Geological Society of America, pp 55–76
- Horwell CJ, Williamson BJ, Llewellyn EW et al (2013) The nature and formation of cristobalite at the Soufrière Hills volcano, Montserrat: implications for the petrology and stability of silicic lava domes. *Bull Volcanol* 75:1–19
- Houghton BF, Wilson CJN (1989) A vesicularity index for pyroclastic deposits. *Bull Volcanol* 51:451–462. <https://doi.org/10.1007/BF01078811>
- Houghton BF, Wilson CJN, Del Carlo P et al (2004) The influence of conduit processes on changes in style of basaltic Plinian eruptions:

- Tarawera 1886 and Etna 122 BC. *J Volcanol Geotherm Res* 137:1–14. <https://doi.org/10.1016/j.jvolgeores.2004.05.009>
- Komorowski J-C, Legendre Y, Christopher T et al (2010) Insights into processes and deposits of hazardous vulcanian explosions at Soufrière Hills Volcano during 2008 and 2009 (Montserrat, West Indies). *Geophys Res Lett* 37:1–6. <https://doi.org/10.1029/2010GL042558>
- Lavallée Y, Varley NR, Alatorre-Ibargüengoitia MA et al (2012) Magmatic architecture of dome-building eruptions at Volcán de Colima, Mexico. *Bull Volcanol* 74:249–260. <https://doi.org/10.1007/s00445-011-0518-4>
- Maeno F, Nakada S, Yoshimoto M et al (2019) A sequence of a Plinian eruption preceded by dome destruction at Kelud volcano, Indonesia, on February 13, 2014, revealed from tephra fallout and pyroclastic density current deposits. *J Volcanol Geotherm Res* 382:24–41. <https://doi.org/10.1016/j.jvolgeores.2017.03.002>
- Manga M, Mitchell SJ, Degruyter W, Carey RJ (2018) Transition of eruptive style: pumice raft to dome-forming eruption at the Havre submarine volcano, southwest Pacific Ocean. *Geology* 46:1075–1078. <https://doi.org/10.1130/G45436.1>
- Manrique N, Samaniego P, Médard E et al (2020) Pre-eruptive magmatic processes associated with the historical ( $218 \pm 14$  aBP) explosive eruption of Tutupaca volcano (southern Peru). *Bull Volcanol* 82:6. <https://doi.org/10.1007/s00445-019-1335-4>
- Massaro S, Sulpizio R, Costa A et al (2018) Understanding eruptive style variations at calc-alkaline volcanoes: the 1913 eruption of Fuego de Colima volcano (Mexico). *Bull Volcanol* 80:62. <https://doi.org/10.1007/s00445-018-1235-z>
- Miller TP (1994) Dome growth and destruction during the 1989–1990 eruption of Redoubt Volcano. *J Volcanol Geotherm Res* 62:197–212. [https://doi.org/10.1016/0377-0273\(94\)90034-5](https://doi.org/10.1016/0377-0273(94)90034-5)
- Miyabuchi Y, Hanada D, Niimi H, Kobayashi T (2013) Stratigraphy, grain-size and component characteristics of the 2011 Shinmoe-dake eruption deposits, Kirishima Volcano, Japan. *J Volcanol Geotherm Res* 258:31–46. <https://doi.org/10.1016/j.jvolgeores.2013.03.027>
- Mujin M, Nakamura M (2014) A nanolite record of eruption style transition. *Geology* 42:611–614. <https://doi.org/10.1130/G35553.1>
- Nguyen CT, Gonnermann HM, Houghton BF (2014) Explosive to effusive transition during the largest volcanic eruption of the 20th century (Novarupta 1912, Alaska). *Geology* 42:703–706. <https://doi.org/10.1130/G35593.1>
- Nocquet J-M, Villegas-Lanza JC, Chlieh M et al (2014) Motion of continental slivers and creeping subduction in the northern Andes. *Nat Geosci* 7:287–291. <https://doi.org/10.1038/ngeo2099>
- Padrón E, Hernández PA, Toulkeridis T et al (2008) Diffuse CO<sub>2</sub> emission rate from Pululahuá and the lake-filled Cuicocha calderas, Ecuador. *J Volcanol Geotherm Res* 176:163–169. <https://doi.org/10.1016/j.jvolgeores.2007.11.023>
- Papale P, Rosi M (1993) A case of no-wind plinian fallout at Pululagua caldera (Ecuador): implications for models of clast dispersal. *Bull Volcanol* 55:523–535. <https://doi.org/10.1007/BF00304594>
- Pidgen A (2014) Cuicocha Volcano, Ecuador: reconstruction of major explosive phases through investigation of associated pyroclastic deposits. Master Thesis, University of Oxford
- Preece K, Gertisser R, Barclay J et al (2016) Transitions between explosive and effusive phases during the cataclysmic 2010 eruption of Merapi volcano, Java, Indonesia. *Bull Volcanol* 78:54. <https://doi.org/10.1007/s00445-016-1046-z>
- Ramon P, Vallejo S, Mothes P et al (2021) Instituto Geofísico – Escuela Politécnica Nacional, the Ecuadorian Seismology and Volcanology Service. *Volcanica* 4:93–112. <https://doi.org/10.30909/vol.04.S1.93112>
- Ridolfi F, Renzulli A (2012) Calcic amphiboles in calc-alkaline and alkaline magmas: thermobarometric and chemometric empirical equations valid up to 1,130° C and 2.2 GPa. *Contrib Mineral Petrol* 163:877–895
- Riker JM, Cashman KV, Rust AC, Blundy JD (2015) Experimental constraints on plagioclase crystallization during H<sub>2</sub>O- and H<sub>2</sub>O-CO<sub>2</sub>-saturated magma decompression. *J Petrol* 56:1967–1998
- Robin C, Eissen J-P, Samaniego P et al (2009) Evolution of the late Pleistocene Mojanda-Fuya Fuya volcanic complex (Ecuador), by progressive adakitic involvement in mantle magma sources. *Bull Volcanol* 71:233–258
- Robin C, Hall M, Jimenez M et al (1997) Mojanda volcanic complex (Ecuador): development of two adjacent contemporaneous volcanoes with contrasting eruptive styles and magmatic suites. *J South Am Earth Sci* 10:345–359
- Robin C, Samaniego P, Le Pennec J-L et al (2008) Late Holocene phases of dome growth and Plinian activity at Guagua Pichincha volcano (Ecuador). *J Volcanol Geotherm Res* 176:7–15. <https://doi.org/10.1016/j.jvolgeores.2007.10.008>
- Schindelin J, Arganda-Carreras I, Frise E et al (2012) Fiji: an open-source platform for biological-image analysis. *Nat Methods* 9:676–682
- Schipper CI, Castro JM, Tuffen H et al (2015) Cristobalite in the 2011–2012 Cordón Caulle eruption (Chile). *Bull Volcanol* 77:1–19
- Smithsonian Institution (2021) Pululahuá, General Information. In: Smithsonian. Inst. Natl. Mus. Nat. Hist. Glob. Volcanism Program. <https://volcano.si.edu/volcano.cfm?vn=352011>. Accessed 14 May 2021
- Sulpizio R, Mele D, Dellino P, La Volpe L (2007) Deposits and physical properties of pyroclastic density currents during complex Subplinian eruptions: the AD 472 (Pollena) eruption of Somma-Vesuvius, Italy. *Sedimentol* 54:607–635. <https://doi.org/10.1111/j.1365-3091.2006.00852.x>
- Turbeville BN, Waresback DB, Self S (1989) Lava-dome growth and explosive volcanism in the Jemez Mountains, New Mexico: evidence from the Plio-Pleistocene Puye alluvial fan. *J Volcanol Geotherm Res* 36:267–291. [https://doi.org/10.1016/0377-0273\(89\)90074-7](https://doi.org/10.1016/0377-0273(89)90074-7)
- Villemant B, Boudon G (1998) Transition from dome-forming to plinian eruptive styles controlled by H<sub>2</sub>O and Cl degassing. 392:5
- Villemant B, Boudon G, Komorowski J-C (1996) U-series disequilibrium in arc magmas induced by water-magma interaction. *Earth Planet Sci Lett* 140:259–267. [https://doi.org/10.1016/0012-821X\(96\)00035-0](https://doi.org/10.1016/0012-821X(96)00035-0)
- Vogel A, Diplas S, Durant AJ et al (2017) Reference data set of volcanic ash physicochemical and optical properties. *J Geophys Res Atmospheres* 122:9485–9514
- Volentik ACM, Bonadonna C, Connor CB et al (2010) Modeling tephra dispersal in absence of wind: insights from the climactic phase of the 2450BP Plinian eruption of Pululagua volcano (Ecuador). *J Volcanol Geotherm Res* 193:117–136. <https://doi.org/10.1016/j.jvolgeores.2010.03.011>
- Wadge G, Voight B, Sparks RSJ et al (2014) An overview of the eruption of Soufrière Hills Volcano, Montserrat from 2000 to 2010. *Geol Soc Lond Mem* 39:1–40
- Witt C, Bourgeois J, Michaud F et al (2006) Development of the Golfo de Guayaquil (Ecuador) as an effect of the North Andean block tectonic escape since the Lower Pleistocene. *Tectonics* 25:TC3017
- Wright HM, Cashman KV, Rosi M, Cioni R (2007) Breadcrust bombs as indicators of Vulcanian eruption dynamics at Guagua Pichincha volcano, Ecuador. *Bull Volcanol* 69:281–300

Springer Nature or its licensor holds exclusive rights to this article under a publishing agreement with the author(s) or other rightsholder(s); author self-archiving of the accepted manuscript version of this article is solely governed by the terms of such publishing agreement and applicable law.